Peristaltic pumping and irreversibility of a Stokesian viscoelastic fluid

Joseph Teran,[1] Lisa Fauci,[2] and Michael Shelley[1]

[1]*Courant Institute of Mathematical Sciences, New York University, New York City, New York 10012, USA*

[2]*Department of Mathematics, Tulane University, New Orleans, Louisiana 70118, USA*

Peristaltic pumping by wavelike contractions is a fundamental biomechanical mechanism for fluid and material transport and is used in the esophagus, intestine, oviduct, and ureter. While peristaltic pumping of a Newtonian fluid is well understood, in many important settings, as in the fluid dynamics of reproduction, the fluids have non-Newtonian responses. Here, we present a numerical method for simulating an Oldroyd-B fluid coupled to contractile, moving walls. A marker and cell grid-based projection method is used for the fluid equations and an immersed boundary method is used for coupling to a Lagrangian representation of the deforming walls. We examine numerically the peristaltic transport of a highly viscous Oldroyd-B fluid over a range of Weissenberg numbers and peristalsis wavelengths and amplitudes. © *2008 American Institute of Physics.*
[DOI: 10.1063/1.2963530]

I. INTRODUCTION

Problems in biological fluid dynamics typically involve the interaction of an elastic structure with a surrounding fluid. Sperm motility in the reproductive tract and peristaltic contractions of the ureter and oviduct are examples of such interactions. For Newtonian fluids, there has been considerable progress in formulating mathematical descriptions and numerical algorithms for the simulation of these coupled systems. However, many biological fluids are actually complex; that is, they are not liquids or mixtures of a simple molecular structure that yield Newtonian responses but instead have complicated non-Newtonian mechanical responses that arise, usually, because they have suspended microstructures. These complex fluids bring important new physics to even classical problems in biological fluid dynamics. In this manuscript we describe a mathematical model and numerical method that couples a moving boundary to a Stokes–Oldroyd-B (OB) description of an elastic Boger fluid using an immersed boundary framework. Other immersed boundary simulations have captured viscoelastic effects in the fluid domain. For instance, in Ref. 1 Fogelson tracked a concentration of interplatelet links within a macroscopic fluid in a continuum model of platelet aggregation. While we will focus on the classical fluid dynamics problem of peristaltic pumping in a two-dimensional (2D) channel, we will also demonstrate that the reversibility of Stokes flow is lost in this non-Newtonian case. We will compare fundamental aspects of pumping in the cases of Newtonian and OB peristaltic pumping. Most notably, we will show that the optimal flow produced with varying occlusion ratio (of the wave amplitude to the channel separation) is fundamentally different for Newtonian and OB model fluids. Newtonian fluids produce increasing flow as the ratio approaches complete occlusion; however Olrdroyd-B fluids produce decreasing flow as the occlusion ratio goes beyond a critical value far short of complete occlusion.

A. Peristalsis

Waves of contraction passed along a fluid bearing tube result in net transport of the fluid in the wave direction. This peristaltic pumping is responsible for many physiological flows, including urodynamics in the renal pelvis[2] and rapid sperm transport from the uterus to the oviducts,[3] and contributes to ovum transport in the oviduct.[4] Oviductal mucosal fluid demonstrates non-Newtonian properties.[5]

In some instances of peristaltic pumping, fluid transport is also affected by an applied pressure gradient along the channel. This gradient can act against the mechanical wave and cause reflux, the transport of particles in the direction opposite that of the wave. In the context of *in vitro* fertilization, Eytan *et al.*[6] asserted that this fluid mechanical phenomenon of reflux is the cause of unsuccessful embryo implantation in women who suffer from hydrosalpinx, a tubal pathology that causes accumulation of fluid in the oviduct. This increases tubal pressure and results in an applied pressure gradient that acts against the peristaltic wave in the uterus that would otherwise transport the embryo to an appropriate implantation site at the fundus. Surgical removal of the oviduct with hydrosalpinx to improve implantation chances remains a controversial issue.[6]

There have been many mathematical and computational models developed to describe fluid flow in a tube undergoing peristalsis with prescribed wall motions. In earlier analytical studies, simplifying assumptions were made, including small amplitude oscillations, long wavelength, as well as symmetry of the channel (e.g., Refs. 7 and 8). Subsequent studies have been less restrictive and have captured features such as finite wavelength, nonuniform channel geometry, as well as effects of finite length channels (e.g., Refs. 9–13). Recently, there have been coordinated experimental, mathematical and computational studies of uterine peristalsis.[6,14–17]
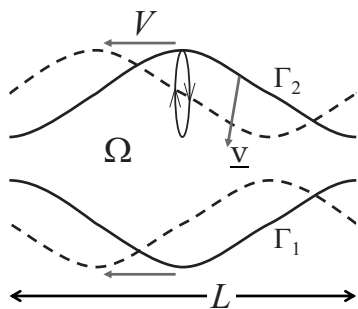
FIG. 1. Peristaltic pumps work by propagating a contractile wave with speed V along an elastic fluid boundary. Though the wave propagates in the direction of the bulk fluid flow, the motions of the material points in the boundary are primarily lateral (shown moving with speed v in the figure). The figure depicts such a mechanisms with Γ_1 and Γ_2 depicting the lower and upper elastic boundaries, respectively.

II. THE VISCOELASTIC FLOW MODEL

We shall consider peristaltic pumping in the x-periodic geometry illustrated in Fig. 1. Here L is the periodicity length. The two walls Γ_1 and Γ_2 will move through the set of shapes given by $[x, \pm y_{\text{wall}}(x+Vt)]$, where y_{wall} is an L-periodic function of its argument and V is the speed of the left-moving wave. The velocity of the wall is then $v_{1,2} = \pm V y'_{\text{wall}}$. Note that the wall does not move as an inextensible surface but rather stretches and compresses as the wave of deformation moves through it.

We have chosen the OB equations as our viscoelastic flow model. This model arises from a simple conception of the microscopic origin of viscoelasticity. Here, one considers a dilute suspension of high molecular weight polymers in a Newtonian solvent where the ceaseless collisions of solvent molecules cause the molecule to roughly conform to a random walk. The polymer molecules' distortions from equilibrium are represented by the distribution of the end-to-end displacement vector $\mathbf{R}$. Assuming that the polymer coil responds to deformation as a linear Hookean spring, one can show using Kirkwood's formula that the additional or *extra* stress to the solvent stress provided by the distended polymers is given by

$$\mathbf{S}_p = \alpha \langle \mathbf{R}\mathbf{R}^T \rangle, \tag{1}$$

where $\langle \cdot \rangle$ represents a distributional average over a fluid volume.[18] Hence, in this case the extra stress is essentially a sum of outer-product matrices.

This simple microscopic picture yields the OB equations

$$\rho \frac{D\mathbf{u}}{Dt} = \nabla \cdot (\mathbf{S}_s + \mathbf{S}_p) \quad \text{and} \quad \nabla \cdot \mathbf{u} = 0 \quad \text{in } \Omega,$$

with $\mathbf{u}|_{\Gamma_{1,2}} = \mathbf{v}$,

$$\tau \mathbf{S}_p^\nabla = -(\mathbf{S}_p - G\mathbf{I}) \quad \text{in } \Omega,$$

where $\mathbf{S}_s$ is the usual Newtonian (solvent) stress tensor $\mathbf{S}_s = -p\mathbf{I} + 2\mu\mathbf{E}$ ($\mathbf{E}$ is the symmetric rate-of-strain tensor), τ is the time scale for polymer relaxation, and $G\mathbf{I}$ is the additional isotropic stress in the fluid arising from thermodynamic fluctuations of the polymer chains.[18] The upper convected time derivative, $\mathbf{S}^\nabla$, is defined by

$$\mathbf{S}^\nabla \equiv \frac{D\mathbf{S}}{Dt} - (\nabla\mathbf{u}\mathbf{S} + \mathbf{S}\,\nabla\,\mathbf{u}^T) \tag{2}$$

and is a natural transport operator for such a tensor.

The period length L of the pump section (see Fig. 1) is taken as a characteristic length scale, and V as a characteristic velocity, giving $\tau_f = L/V$ as a characteristic flow time scale. To make the equations adimensional, we take G as the scale of $\mathbf{S}_p$ and the pressure scale as $P = \mu/\tau_f$. We then have

$$\text{Re}\,\frac{D\mathbf{u}}{Dt} = -\nabla p + \nabla\mathbf{u} + \beta\nabla\cdot\mathbf{S}_p \quad \text{and} \quad \nabla\cdot\mathbf{u} = 0 \quad \text{in } \Omega,$$

with $\mathbf{u}|_{\Gamma_{1,2}} = \mathbf{v}$,

$$Wi\mathbf{S}_p^\nabla = -(\mathbf{S}_p - \mathbf{I}) \quad \text{in } \Omega,$$

where $\text{Re} = \rho V L/\mu$ is the Reynolds number, $Wi = \tau/\tau_f$ is the Weissenberg number, and $\beta = G\tau_f/\mu$ is the (adimensional) strength of feedback of the polymer stress to the momentum balance equation. Note that the flow time scale τ_f is chosen so that the boundary velocity is order 1.

We study this system in the limit where Re is small; yet Wi is at least order 1. This yields the Stokes-OB equations

$$-\nabla p + \Delta\mathbf{u} = -\beta\nabla\cdot\mathbf{S}_p \quad \text{and} \quad \nabla\cdot\mathbf{u} = 0 \quad \text{in } \Omega, \tag{3}$$

with $\mathbf{u}|_{\Gamma_{1,2}} = \mathbf{v}$,

$$\mathbf{S}_p^\nabla = -Wi^{-1}(\mathbf{S}_p - \mathbf{I}) \quad \text{in } \Omega. \tag{4}$$

Hence, given the gradients of polymer stress, Eq. (3) constitutes a Stokes boundary value problem for the velocity $\mathbf{u}$. The polymer stress is advected and damped via the transport equation (4).

Since there is no scale-dependent dissipation operative in Eq. (4), no boundary conditions are necessary for $\mathbf{S}_p$ at $\Gamma_{1,2}$. This is made clearer by rewriting Eq. (4) in the Lagrangian frame,

$$(\mathbf{F}^{-1}\mathbf{S}_p\mathbf{F}^{-T})_t = -Wi^{-1}(\mathbf{F}^{-1}\mathbf{S}_p\mathbf{F}^{-T} - \mathbf{F}^{-1}\mathbf{F}^{-T}). \tag{5}$$

Here $\mathbf{F} = \partial\phi/\partial\mathbf{X}$ is the so-called deformation tensor or the Jacobian of the Lagrangian flow map ϕ. The flow map gives the time t location of particle $\mathbf{X}$ of the material and its time derivative is the material velocity. Equation (5) shows that the evolution of $\mathbf{S}$ requires only local information about $\mathbf{S}$ along a Lagrangian path. Because of its provenance as a sum of tensors of the form $\mathbf{R}\mathbf{R}^T$, $\mathbf{S}_p$ should be a symmetric positive definite (spd) tensor. Indeed one can show that if $\mathbf{S}_p$ is initially spd, then Eq. (5) will preserve this property.

The Newtonian Stokes equations are recovered in the limit $Wi \to 0$, in which case the polymer stress is uniform and isotropic. In the formal limit $Wi \to \infty$ the system becomes that for a neo-Hookean solid with a viscous stress response.

The Stokes-OB equations have a natural energy law. Let

$$\mathcal{E} = \frac{1}{2}\int_\Omega \text{trace}(\mathbf{S}_p - \mathbf{I}).$$

Then

$$\dot{\mathcal{E}} + Wi^{-1}\mathcal{E} = -\beta^{-1}\int_{\Omega}|\nabla\mathbf{u}|^2 + \int_{\Gamma_1+\Gamma_2}\mathbf{v}\cdot(\beta^{-1}\mathbf{S}_s + \mathbf{S}_p)\cdot\hat{\mathbf{n}}.$$

(6)

The first term on the right-hand side is the rate of viscous energy dissipation, while the second term gives the rate of work being done by the boundary motion upon the fluid. Note that for fixed β, there is energy decay even in the limit of infinite Wi owing to the viscous response of the Newtonian solvent.

We note that the product $\beta Wi = G\tau/\mu$ is the ratio of the polymer viscosity to solvent viscosity and thus is a material quantity of the fluid and independent of experimental conditions. As a point of comparison, from the paper of Arratia *et al.*[19] the solution viscosity is 1.2 Pa s, while that of the solvent (97% glycerol/water) is 0.8 Pa s. This yields $\beta Wi = (1.2-0.8)/0.8 = 0.5$. In the simulations presented here, we set $\beta Wi = \frac{1}{2}$ so as to fix the material being modeled.

Reversibility. A fundamental aspect of the Newtonian Stokes equations is their exact reversibility under a variety of conditions. Of relevance here is reversibility under a reversal of boundary motion. That is, if $V \to -V$ then $\mathbf{u} \to -\mathbf{u}$. There are two related consequences to this. One is that if the fluid is pumped forward, some number of cycles and the direction of the peristalsis are reversed for the same number of cycles; the fluid will return exactly to its original position. The second is that, regardless of the wall shape, the efficiency of pumping is unaffected by the direction of peristalsis. Neither of these two features remain true for the Stokes-OB system. These facts are signaled directly by the existence of an energy decay law reflecting the history dependence in the system.

III. METHODS

We model the pumping of an OB fluid due to a peristaltic, traveling wave passed along the walls of a 2D, spatially periodic channel. Following Ref. 20, we use the immersed boundary method to capture the coupled fluid-structure interactions between the moving channel walls and the surrounding fluid, although here the governing equations model a complex Stokes-OB fluid in the Stokesian regime rather than a Newtonian one at nonzero Reynolds number. In order to model the peristaltic channel, we choose our computational domain Ω' to be a square whose side length is one wavelength of the contractile channel. The channel walls extend from one side of the domain to the other, and periodic boundary conditions are imposed upon the fluid dynamic equations and wall motions. The flow domain $\Omega \in \Omega'$ is the region between the two walls. The flow in the region complementary to Ω is also that of a peristaltic pump, but with our choice of geometric parameters defining the walls, the geometric shape and consequent flow in the complementary region are identical to that in Ω.

In the immersed boundary framework, the governing equations are

$$0 = \Delta\mathbf{u} - \nabla p + \beta\nabla\cdot\mathbf{S} + \mathbf{f},$$

$$\nabla\cdot\mathbf{u} = 0,$$

$$\frac{D\mathbf{S}}{Dt} = \nabla\mathbf{u}\cdot\mathbf{S} + \mathbf{S}\cdot\nabla\mathbf{u}^T + \frac{1}{Wi}(\mathbf{I} - \mathbf{S}),$$

$$\mathbf{f}(\mathbf{x}) = \int_{\Gamma}\mathbf{F}[\mathbf{X}(\xi,t)]\delta(\mathbf{x} - \mathbf{X}(\xi,t))d\xi,$$

$$\frac{\partial\mathbf{X}}{\partial t} = \int_{\Omega'}\mathbf{u}(\mathbf{x})\delta(\mathbf{x} - \mathbf{X}(\xi,t))d\mathbf{x}.$$

Here, $\mathbf{X}(\xi,t)$ is the configuration of the Lagrangian boundary $\Gamma = \Gamma_1 + \Gamma_2$ at time t, $\mathbf{S} = \mathbf{S}_p$ in Eq. (4), $\delta(\mathbf{x})$ is the 2D Dirac delta function, $\mathbf{F}$ is the elastic force per unit length along the channel walls, and $\mathbf{f}$ is the force per unit area, which is exerted on the fluid domain Ω by the walls of the channel. Following the immersed boundary framework,[21] this force on the fluid is a δ-function layer supported only by the region of fluid which coincides with material points of the channel walls; away from these points the force is zero. Our coupled fluid-immersed boundary system is closed by requiring that the velocity of a material point of a channel wall be equal to the fluid velocity evaluated at that point.

In order to impose prescribed motion of the channel walls, we choose the Lagrangian force $\mathbf{F}$ to be

$$\mathbf{F} = -\hat{k}[\mathbf{X}(\xi,t) - \mathbf{Z}(\xi,t)].$$

These forces can be interpreted as elastic forces due to Hookean springs with zero rest lengths connecting the wall points $\mathbf{X}(\xi,t)$ to specified "tether" points $\mathbf{Z}(\xi,t)$. The stiffness constant $\hat{k}$ is a numerical parameter that is chosen as large as possible in order to (approximately) enforce the prescribed wall motions. The prescribed wall motion, in adimensional units, is $\mathbf{Z}(\xi,t) = \{(\xi, 0.5 + d(\xi,t))\,|\,\xi \in [0,1]\} \cup \{(\xi, 0.5 - d(\xi,t))\,|\,\xi \in [0,1]\}$. Here d is typically a sinusoidal wave,

$$d(\xi,t) = \frac{\alpha}{2\pi}[1 + \chi\sin 2\pi(\xi - t)].$$

Here α measures the aspect ratio of the channel, while χ measures the wave amplitude to channel width ratio: for $\chi = 0$ the channel is straight, while for $\chi = 1$ it is completely occluded.

A. Compatibility conditions in a periodic domain

Our use of periodic boundary conditions necessitates that all forces integrate to zero over the domain Ω',

$$\int_{\Omega'}[\mathbf{f} + \beta\nabla\cdot\mathbf{S}]d\mathbf{x} = \mathbf{0}.$$

The assumption of periodicity for the elastic stress $\mathbf{S}$ ensures that the polymer-based forces integrate to zero. Therefore, we require that the tether forces integrate to zero. Periodic boundary conditions have the additional consequence that the velocity field is defined only up to an additive constant $\mathbf{u}_c$ and so we may write

$$\mathbf{u} = \hat{\mathbf{u}} + \mathbf{u}_c \quad \text{where} \quad \int_{\Omega'} \hat{\mathbf{u}} d\mathbf{x} = 0.$$

For Stokes flow, a constant velocity field $\mathbf{u}_c$ can be uniquely determined when using the immersed boundary method with tether forces to ensure that these forces always integrate to zero over the domain. We can use this same constant velocity determination here for the Stokes-OB system,

$$\mathbf{u}_c = \frac{-1}{\int_\Gamma d\xi} \left[\int_\Gamma \left(\int_{\Omega'} \hat{\mathbf{u}} \delta(\mathbf{x} - \mathbf{X}) d\mathbf{x} - \frac{\partial \mathbf{Z}}{\partial t} \right) d\xi \right]. \quad (7)$$

This constant velocity is determined by requiring that the time derivative of the integral of the tether forces is zero. Hence, if initially the tether forces do integrate to zero, they will continue to integrate to zero.

When discretized in time, at the beginning of the nth time step, the state of the system is given by the configuration of the immersed boundary walls $\mathbf{X}^n$ and the polymer stress tensor $\mathbf{S}^n$. In order to update the configuration of the immersed boundary walls, we must compute $\mathbf{u}^n = \hat{\mathbf{u}}^n + \mathbf{u}_c^n$ while ensuring that the tether forces at time $n+1$ integrate to zero. We do this by first computing the portion of the velocity that integrates to zero $\hat{\mathbf{u}}^n$ and its effect on the immersed boundary $\hat{\mathbf{X}}^{n+1}$ as

$$\Delta \hat{\mathbf{u}}^n = \nabla p^n - \mathbf{f}^n + \beta \nabla \cdot \mathbf{S}^n,$$

$$\nabla \cdot \hat{\mathbf{u}}^n = 0,$$

$$\hat{\mathbf{X}}^{n+1} = \mathbf{X}^n + \Delta t \int_{\Omega'} \hat{\mathbf{u}}^n \delta(\mathbf{x} - \mathbf{X}^n) d\mathbf{x}.$$

The velocity $\mathbf{u}_c^n$ and immersed boundary configuration $\mathbf{X}^{n+1}$ are then determined in a way that ensures the forces at time $n+1$ integrate to zero,

$$\mathbf{u}_c^n = \frac{1}{\int_\Gamma d\xi} \left(\hat{k} \int_\Gamma \frac{\mathbf{Z}^{n+1} - \hat{\mathbf{X}}^{n+1}}{\Delta t} d\xi \right),$$

$$\mathbf{X}^{n+1} = \hat{\mathbf{X}}^{n+1} + \Delta t \mathbf{u}_c^n. \quad (8)$$

This velocity is a first-order approximation to the continuous value in Eq. (7) and ensures that the forces integrate to zero at time $n+1$. In the following subsections, we describe the numerical methods used to evolve the fluid and polymer stress equations.

B. Spatial discretization

We rewrite the Stokes equations, introducing an intermediate velocity $\mathbf{u}^*$ and scalar function $\hat{p}$ as

$$\Delta \mathbf{u}^* = -\mathbf{f} - \beta \nabla \cdot \mathbf{S}, \quad (9)$$

$$\Delta \hat{p} = \nabla \cdot \mathbf{u}^*, \quad (10)$$

$$\hat{\mathbf{u}} = \mathbf{u}^* - \nabla \hat{p}, \quad (11)$$

where the scalar $\hat{p}$ satisfies $p = -\Delta \hat{p}$. In this way, for a given stress tensor $\mathbf{S}$ and immersed boundary force field $\mathbf{f}$, we may
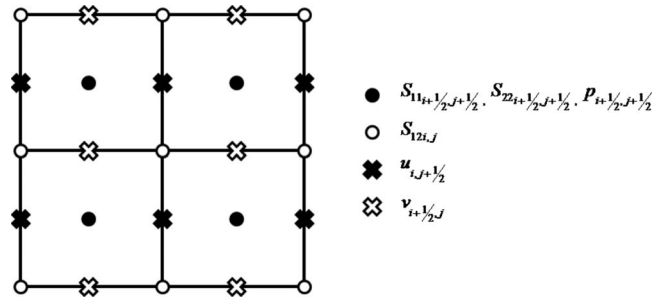

FIG. 2. A MAC grid cell stores pressure and diagonal stress components at cell centers, x velocity components on horizontal faces, y velocity components on vertical faces, and off-diagonal component of the stress at the corners.

solve for the fluid velocity field and pressure by solving two Poisson equations with periodic boundary conditions on the domain Ω'.

We use a marker and cell (MAC) grid structure when solving the Poisson equations (9) and (10) for the fluid velocity and pressure as in Ref. 22 (see Fig. 2). With this structure, we decompose a uniform Eulerian grid into three separate components with the x components of the velocity ($u_{i+1/2,j}$) defined on horizontal faces of each cell, the y components ($v_{i,j+1/2}$) on the vertical faces, and the diagonal stress components ($p_{i,j}, \hat{p}_{i,j}, S_{11}|_{i,j}, S_{22}|_{i,j}$) defined at the cell centers. $\nabla \cdot \mathbf{u}^*$ is then naturally defined at the cell centers when solving for $\hat{p}$. Using a standard five-point stencil, we get the following system of equations:

$$\frac{\hat{p}_{i+1,j} + \hat{p}_{i-1,j} + \hat{p}_{i,j+1} + \hat{p}_{i,j-1} - 4\hat{p}_{i,j}}{h^2}$$

$$= \frac{u^*_{i+1/2,j} - u^*_{i-1/2,j}}{h} + \frac{v^*_{i,j+1/2} - v^*_{i,j-1/2}}{h}$$

or more compactly

$$L^h \hat{p}_{i,j} = \mathbf{D}_-^h \cdot \begin{pmatrix} u^*_{i+1/2,j} \\ v^*_{i,j+1/2} \end{pmatrix} = \begin{pmatrix} D^h_{x-} \\ D^h_{y-} \end{pmatrix} \cdot \begin{pmatrix} u^*_{i+1/2,j} \\ v^*_{i,j+1/2} \end{pmatrix},$$

where h is the grid spacing in both the x and y directions. $\hat{p}$ is then used to discretely project $\mathbf{u}^*$ to the divergent free $\hat{\mathbf{u}}$ as

$$\hat{u}_{i+1/2,j} = u^*_{i+1/2,j} - \frac{\hat{p}_{i+1,j} - \hat{p}_{i,j}}{h},$$

$$\hat{v}_{i,j+1/2} = v^*_{i,j+1/2} - \frac{\hat{p}_{i,j+1} - \hat{p}_{i,j}}{h}.$$

The MAC based locations of the x and y components of the velocity and their governing equations of motion naturally suggest storing S_{11} and S_{22} at cell centers as with the pressure and S_{12} at the grid corners (see Fig. 2). With this grid structure, the equations for u^* are

$$\frac{u^*_{i+3/2,j} + u^*_{i-1/2,j} + u^*_{i+1/2,j-1} + u^*_{i+1/2,j+1} - 4u^*_{i+1/2,j}}{h^2}$$

$$= f_1|_{i+1/2,j} + \beta\left(\frac{S_{11}|_{i+1,j} - S_{11}|_{i,j}}{h} \right.$$

$$\left. + \frac{S_{12}|_{i+1/2,j+1/2} - S_{12}|_{i+1/2,j-1/2}}{h} \right)$$

or

$$L^h u^*_{i+1/2,j} = f_1|_{i+1/2,j} + \beta(D^h_{x+} S_{11}|_{i,j} + D^h_{y-} S_{12}|_{i+1/2,j+1/2}),$$

where $\mathbf{f} = (f_1, f_2)$. Similarly, v^* is given as

$$L^h v^*_{i,j+1/2} = f_2|_{i,j+1/2} + \beta(D^h_{x-} S_{12}|_{i+1/2,j+1/2} + D^h_{y+} S_{22}|_{i,j}).$$

To solve these systems of equations, we use a conjugate gradient solver with incomplete Chlolesky preconditioner. The velocity field computed here, due to forces that sum to zero, can be shown to have zero average and plays the role of $\hat{\mathbf{u}}$ discussed above.

C. Communication between immersed boundaries and fluid domain

The integrals that communicate forces from the immersed boundaries to the fluid domain and that interpolate the fluid velocity field back to the immersed boundaries each involve the Dirac delta function. The delta function is approximated by a discrete regularized function δ^{IB} defined on the Eulerian grid discretizing Ω'. There are many ways to construct these grid-based approximations that satisfy certain moment conditions.[21] For example, it is very important for the constant velocity calculation ($\mathbf{u}^n_c$) that the discrete approximate delta functions also satisfy the property that integration of a numerically "spread" Lagrangian quantity over the Eulerian domain Ω' be the same as the integral of the quantity over the Lagrangian domain Γ. Such conditions give rise to a family of candidate discrete delta functions, from which we choose a four point delta function δ^{IB}_{4h}. This function has a support of four mesh widths in each spatial direction (i.e., supported over 16 cells in two-dimensions) and is defined in terms of the function ϕ^{IB}_4 with $\delta^{IB}_{4h}(\mathbf{x}) = (1/h^2)\phi^{IB}_4(x/h)\phi^{IB}_4(y/h)$, where

$$\phi^{IB}_4(x) = \begin{cases} \frac{1}{8}(3 - 2|x| + \sqrt{1 + 4|x| - 4x^2}), & |x| \in [0,1] \\ \frac{1}{8}(5 - 2|x| - \sqrt{-7 + 12|x| - 4x^2}), & |x| \in [1,2] \\ 0, & |x| > 2. \end{cases}$$

Using this regularized delta function δ^{IB}_{4h} and a standard second-order quadrature, we can convert Lagrangian forces defined on the immersed boundaries to their Eulerian values on the fluid grid. In the adjoint operation, we can define Lagrangian velocities of the immersed boundary from the Eulerian fluid field $\mathbf{u}$ to couple the wall to the fluid,

$$\mathbf{f}_{i+1/2,j+1/2} = \sum_k \mathbf{F}_k \delta^{IB}_{4h}(\mathbf{x}_{i+1/2,j+1/2} - \mathbf{X}_k)\Delta l_k,$$

$$\mathbf{V}_k = \sum_{i,j} \mathbf{u}_{i+1/2+1/2} \delta^{IB}_{4h}(\mathbf{x}_{i+1/2,j+1/2} - \mathbf{X}_k)h^2,$$

where $\mathbf{X}_k$ are the discrete Lagrangian points that make up the immersed boundaries, $\mathbf{F}_k$ are the Lagrangian forces at points $\mathbf{X}_k$, $\mathbf{V}_k$ are the corresponding velocities, Δl_k are the distances between immersed boundary points, and $\mathbf{x}_{i+1/2,j+1/2}$ are the Eulerian grid node locations. We perform this operation using node based velocities (as implied by the half indexing). These node based velocities are determined with second-order averaging from their incident faces. Additionally, when solving for the intermediate velocity $\mathbf{u}^*$, we need the immersed boundary forces defined on horizontal and vertical faces. This is also done with second-order averaging from the node based $\mathbf{f}_{i+1/2,j+1/2}$. This averaging can be avoided by separately interpolating from and spreading to the horizontal and vertical faces but requires a slightly more involved implementation.

D. Evolution of polymer stress tensor

We adopt a method of line approach to evolving the extra stress tensor. The evolution of the stress tensor $\mathbf{S}$ is governed by the system of differential equations,

$$\frac{\partial \mathbf{S}}{\partial t} = \mathbf{g}(\mathbf{S}, \mathbf{u}), \tag{12}$$

where $\mathbf{g}$ is defined as

$$g_{11}(\mathbf{S}, \mathbf{u}) = 2\left[\frac{\partial u}{\partial x}S_{11} + \frac{\partial u}{\partial y}S_{12} \right] - \frac{\partial S_{11}}{\partial x}u - \frac{\partial S_{11}}{\partial y}v$$

$$+ \frac{1}{Wi}[1 - S_{11}],$$

$$g_{12}(\mathbf{S}, \mathbf{u}) = \frac{\partial u}{\partial y}S_{22} + \frac{\partial v}{\partial x}S_{11} - \frac{\partial S_{12}}{\partial x}u - \frac{\partial S_{12}}{\partial y}v - \frac{S_{12}}{Wi},$$

$$g_{22}(\mathbf{S}, \mathbf{u}) = 2\left[\frac{\partial v}{\partial x}S_{12} + \frac{\partial v}{\partial y}S_{22} \right] - \frac{\partial S_{22}}{\partial x}u - \frac{\partial S_{22}}{\partial y}v$$

$$+ \frac{1}{Wi}[1 - S_{22}].$$

This definition of $\mathbf{g}$ is only valid for divergence-free velocities $\mathbf{u}$.

We use a second-order Runge–Kutta method to evolve $\mathbf{S}$ forward in time,

$$\hat{\mathbf{S}}^{n+1} = S^n + \Delta t \mathbf{g}(\mathbf{S}^n, \mathbf{u}^n),$$

$$\hat{\mathbf{S}}^{n+2} = \hat{\mathbf{S}}^{n+1} + \Delta t \mathbf{g}(\hat{\mathbf{S}}^{n+1}, \mathbf{u}^n),$$

$$\mathbf{S}^{n+1} = \frac{\mathbf{S}^n + \hat{\mathbf{S}}^{n+2}}{2}.$$

When $\mathbf{g}$ is spatially discretized (see Sec. III B), it is apparent that g_{12} is naturally defined at grid nodes (as with S_{12}) and g_{11}, g_{22} are naturally defined at cell centers (as with S_{11} and S_{22}). Computing $\mathbf{g}$ is complicated by the coupling of variables defined at different locations in the grid (faces, corners,

and centers) and second-order interpolation must be performed to accurately define the respective variables where needed.

E. Summary

The state of the system at time step n of the coupled immersed boundary–Stokes-OB system is determined by the stress tensor $\mathbf{S}^n$ and the configuration of the immersed boundary $\mathbf{X}^n$. To advance the system by one time step, we

- use the discretized delta functions to spread the tether forces to the fluid grid to get $\mathbf{f}^n$;
- using $\mathbf{S}^n$, we solve two Poisson problems to determine $\hat{\mathbf{u}}^n$;
- we interpolate this mean-zero velocity field defined on the fluid grid to immersed boundary points $\hat{\mathbf{U}}^n$, using the discretized delta functions, and evolve the immersed boundary points to an intermediate configuration $\hat{\mathbf{X}}^{n+1} = \mathbf{X}^n + \Delta t \hat{\mathbf{U}}^n$;
- we determine the constant velocity field $\mathbf{u}_c^n$ that will assure that the tether forces at the next time step integrate to zero: the fluid velocity field at time level n is then $\mathbf{u}^n = \hat{\mathbf{u}}^n + \mathbf{u}_c^n$ and $\mathbf{X}^{n+1} = \hat{\mathbf{X}}^{n+1} + \Delta t \mathbf{u}_c^n$;
- given $\mathbf{u}^n$, we solve the system of ordinary differential equations for $\mathbf{S}^{n+1}$.

This completes a time step.

Spatial and temporal refinement studies were performed to check the order of accuracy of the scheme. In the presence of an applied, continuous force with no immersed boundary, the above scheme for solving the Stokes-OB system achieves second-order spatial accuracy and second-order temporal accuracy. Inclusion of the immersed boundary reduced the spatial accuracy to first order. As will be shown in the next section, flow rates computed using our immersed boundary Stokes model of peristaltic pumping are virtually identical to those given by asymptotic formulas in the case of very small amplitude pumping.[23] In a related context of propulsion of a swimming sheet in a Stokes-OB fluid, we have compared swimming velocities computed using our immersed boundary Stokes-OB results with the recent asymptotic results of Lauga.[24] Our numerical simulations showed very good agreement with this approximation over a range of fluid and geometric parameters; these comparisons will be reported in a separate manuscript.

IV. RESULTS

Here we show within the comparatively simple Stokes-OB model that complex fluidic responses can cause flow behaviors significantly different from that of a Newtonian fluid. We examine how variations in the amplitude to channel separation ratio χ and Weissenberg number Wi affect the peristaltically driven flow. The 2D Newtonian problem is well studied both asymptotically and numerically and we will use classical results to compare with our numerical model, both as validation and to demonstrate the significantly different behaviors of the complex fluid model.
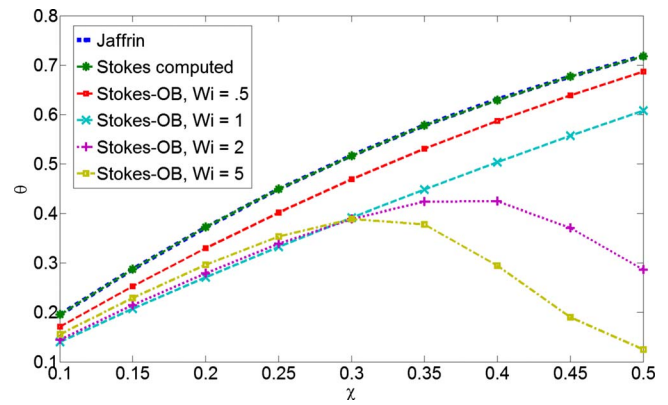

FIG. 3. (Color online) The dimensionless mean flow rate Θ as a function of amplitude ratio χ and Weissenberg number Wi. The top curve compares the asymptotic result of Jaffrin and Shapiro (Ref. 23) with the Newtonian simulation, while the remainder are for nonzero Wi. The flow rate Θ is measured at long times after dependencies on the initial polymer stress distributions have been largely lost.

A. Flow variations with amplitude ratio (χ) and Weissenberg number

The amplitude ratio χ varies between 0 (wide open) and 1 (complete occlusion) and measures the severity of the contractile pumping and the curvature of the domain. For a Newtonian fluid, the mass flux induced by the pump increases monotonically with χ. To quantify the effect of this parameter on the Stokes-OB fluid, we first define

$$Q(x,t) = \int_{0.5-d(x,t)}^{0.5+d(x,t)} u(x,y)dy.$$

Hence, Q is the mass flux across the channel at a fixed station in the laboratory frame. We average (and normalize) this quantity over time (i.e., as waves of peristalsis pass by) and define a dimensionless mean flow rate Θ as

$$\Theta = \frac{1}{2\alpha\chi(T_2 - T_1)} \int_{T_1}^{T_2} Q(x,t)dt,$$

where $\alpha = 2\pi h/L$ and h is the vertical distance between the center of each peristaltic wave. The asymptotic analysis of Jaffrin et al.[25] for a Stokes fluid showed that to zeroth order in $\alpha \ll 1$ (i.e., a long-wave expansion) the dimensionless mean flow rate is

$$\Theta_S = \frac{3\chi}{2 + \chi^2}.$$

Jaffrin and Shapiro later improved upon this result in Ref. 23 by including second-order effects in α to yield

$$\Theta_J = \frac{15\chi^2 + 2\alpha^2[4(1 - \chi^2)^{5/2} + (7\chi^2 - 4)(1 - \chi^2)]}{\chi[5(2 + \chi^2) + 6\alpha^2\chi^2(1 - \chi^2)]}.$$

Figure 3 compares our computed dimensionless mean flow rate with Θ_J for varying χ. Setting β to zero gives the Stokes equations for the velocity and the figure shows excellent agreement with Jaffrin and Shapiro's predicted value in this case. As has been previously noted,[20] Jaffrin and Shapiro's second-order result does extremely well in predicting the
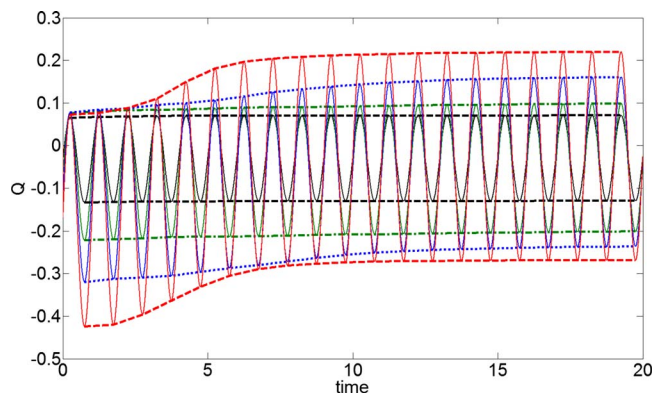
FIG. 4. (Color online) The mean velocity $Q(x=0,t)$ for $Wi=5$ and for χ $=0.1$ (black, dashed curve), 0.2 (yellow, almost completely covered by black curve), 0.3 (green, dashed and dotted curve), 0.4 (blue, dotted curve), and 0.5 (red, dashed curve). The basic dynamics is one of the oscillation on the pump period of unity. To aid the eye in discerning the temporal change in mean value, the envelope of the oscillation is also plotted.

mass flux well outside of its range of formal validity as a long-wave expansion and, indeed, our computed flow rates and Jaffrin and Shapiro's analytic expression are virtually indistinguishable in Fig. 3. While for Stokes-OB the dynamical evolution of the polymer stress is of central importance, for calculating the average flux we compute to long times to remove the effects of the initial conditions for polymer stress ($\mathbf{S}_0=\mathbf{I}$). The Weissenberg number gives the appropriate dimensionless time scale for stress relaxation and we find that setting $T_1=3Wi-1$ and $T_2=3Wi$ is sufficient to remove the effects of these specific initial data, with the flow thereafter being more or less the same from period to period (see Fig. 4, discussed below).

The large differences between Newtonian and viscoelastic responses begin to emerge in Fig. 3. For sufficiently small Wi ($Wi=0.5$ and 1), the dimensionless flow rate decreases continuously from the Newtonian case, showing a likewise monotonic increase with increasing occlusion, at least over the range of χ that is simulated. Note that downward displacement of the flow-rate curve is not just the result of increased shear viscosity due to the presence of suspended polymers; for the Newtonian Stokes equations the pump-induced flow is independent of fluid viscosity. For $Wi>2$ the Newtonian-like monotonic behavior with χ at lower Wi is lost, and at larger Wi the flow rates actually achieve their maxima well before complete occlusion, with higher Wi reaching this point earlier in χ, and henceforth the flow rate drops rapidly as occlusion is approached. Another interesting aspect at small χ is the nonmonotonicity of flux with Wi. For smaller Wi, the flux decreases with increasing Wi, but then increases for yet larger Wi. It appears that this behavior persists to vanishing χ. Monotonicity is restored beyond a crossover point $\chi_C \simeq 0.3$.

We found it very difficult to reliably compute long-time flows for χ much larger than 0.5 at these larger Weissenberg numbers. At larger χ the fluid develops very large normal stresses at the walls, pushing them apart. Of course, the appearance of normal stresses at walls is a characteristic and interesting property of elastic fluids, but their growth neces-

sitates the imposition of larger spring constants in the immersed boundary tether forces so as to maintain the kinematic specification of the wall motion. In turn, the time-step size must be reduced to resolve the spring constant time scale, which then limits the ability to complete the simulation.

While we shall investigate the nature of velocity fields and the stresses further below, Fig. 4 gives some indication of how the flow develops in time by plotting $Q(x=0,t)$ as a function of time for $Wi=5$ and for varying χ. Each of the curves shows how Q increases and decreases as waves of peristalsis pass through the channel. At early times, each simulation behaves in an essentially Newtonian fashion as the polymer stress is initially isotropic and uniform and so makes no contribution to the momentum equation (3), and for small χ (i.e., $\chi=0.1,0.2$), the dynamics of Q remains very close to that of the Newtonian case. To aid the eye the envelope of the oscillating Q is also plotted for each case and shows the generally negative average flux that corresponds to leftward pumping. For the larger values of χ (0.3–0.5), internal flows develop that increasingly oppose the direction of the pump, and so the mean flux diminishes in time, an effect that increases in magnitude with increasing χ. This is seen in Fig. 4 in the increasingly upward shift of Q with increasing χ as time increases.

As an illustrative case we consider $Wi=5$ and $\chi=0.5$. Figures 5–8 show the structure of the fluid vorticity and stresses at times $t_0=0.63$, $t_1=t_0+2$, and $t_1=t_0+9$ (from left to right). Figure 5 shows the vorticity field. For a Newtonian fluid, the vorticity contours are time invariant and closely resemble the profile at time t_0. Since for a Newtonian case the flows are reversible, the vorticity field is left-right symmetric about the neck and waist centers. For Stokes-OB the vorticity evolves out of this state, growing in magnitude and yielding the nonsymmetric profiles seen at large $O(Wi)$ times.

Of course, the evolution of vorticity is driven by the evolution of the polymer stress. These stresses change dramatically in magnitude and spatial distribution as time increases, relaxing to near steady states on an $O(Wi)$ time scale, and underlie the decrease in fluid flux through the pump. Figure 6 shows the evolution of S_{11}. Initially uniform (and unity), S_{11} increases in magnitude and at first realizes a singly peaked structure in the neck region. For a Newtonian fluid (and hence for a Stokes-OB fluid at early times), there is a hyperbolic extensional flow that moves with the wave speed slightly downstream of the constriction. This induces the type of stress growth seen for a four-roll mill flow, as most recently studied by Thomases and Shelley[26] for the Stokes-OB equations, and corresponds to the strong stretching of polymer coils along the x-axis. At later times, this single peak bifurcates, forming a high-magnitude double peak in the neck. Like the vorticity, S_{11} shows no left-right symmetries. For the other diagonal stress component S_{22} (Fig. 7) the largest values instead develop in the wide part of the channel, again asymmetrically, and in time concentrate on the opening part of the channel, rightward of the moving constriction, and in the center. An early time feature that persists to later times is the large central peak that corre-
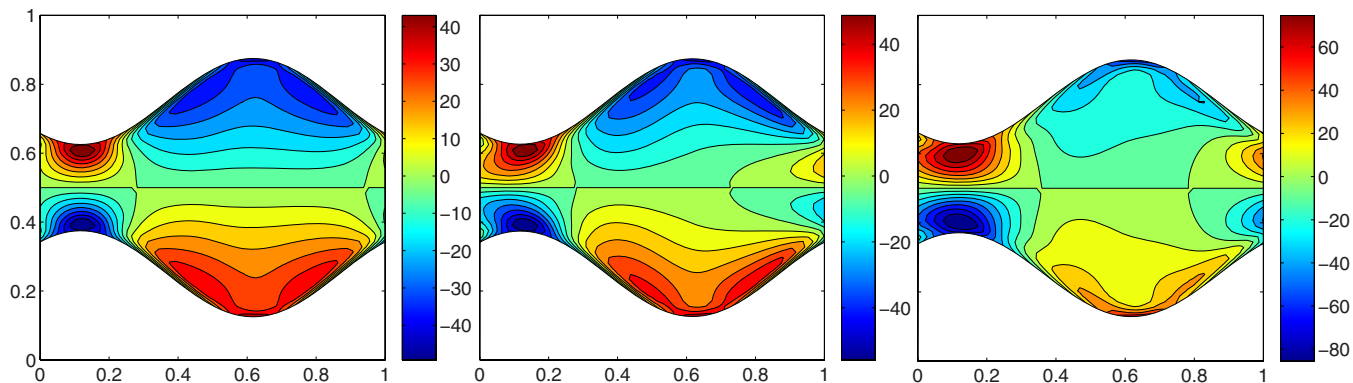
FIG. 5. (Color online) The Stokes-OB fluid vorticity field at times $t_0=0.63$, $t_1=t_0+2$, and $t_2=t_0+9$, as the peristaltic wave moves from right to left. These times are separated by multiples of the pumping period and thus have identical boundary configurations.
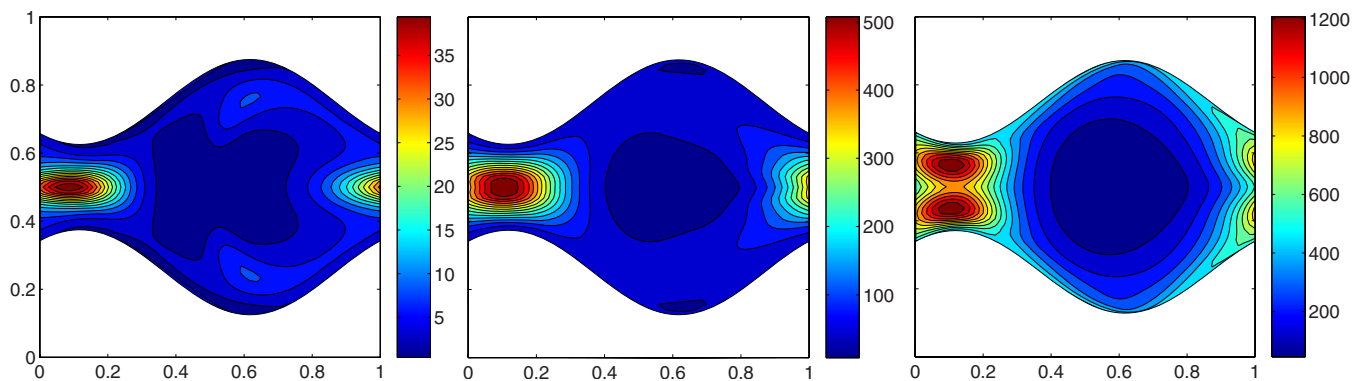

FIG. 6. (Color online) Contours of the polymer stress component S_{11} at times $t_0=0.63$, $t_1=t_0+2$, and $t_2=t_0+9$, as the peristaltic wave moves from right to left.
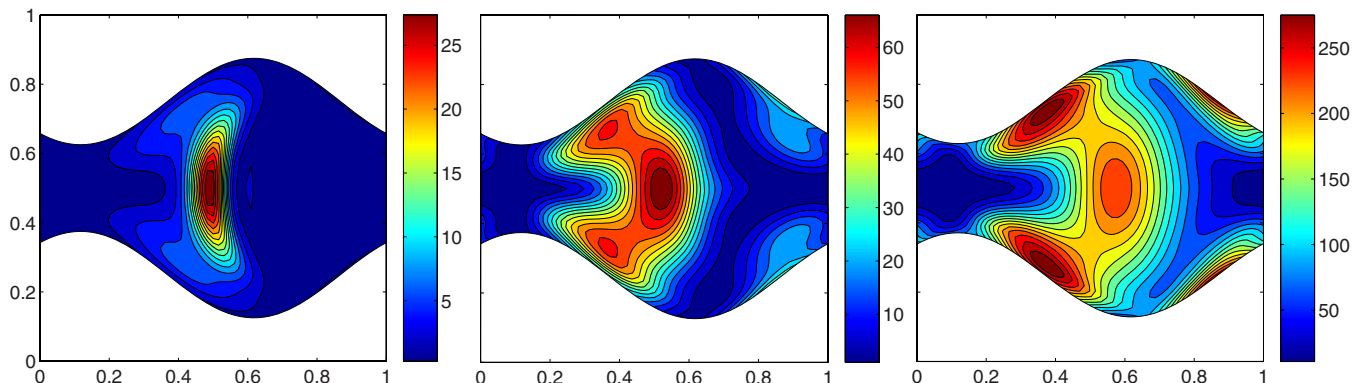

FIG. 7. (Color online) Contours of the polymer stress component S_{22} at times $t_0=0.63$, $t_1=t_0+2$, and $t_2=t_0+9$, as the peristaltic wave moves from right to left.

FIG. 8. (Color online) Contours of the polymer stress component S_{12} at times $t_0=0.63$, $t_1=t_0+2$, and $t_2=t_0+9$, as the peristaltic wave moves from right to left.
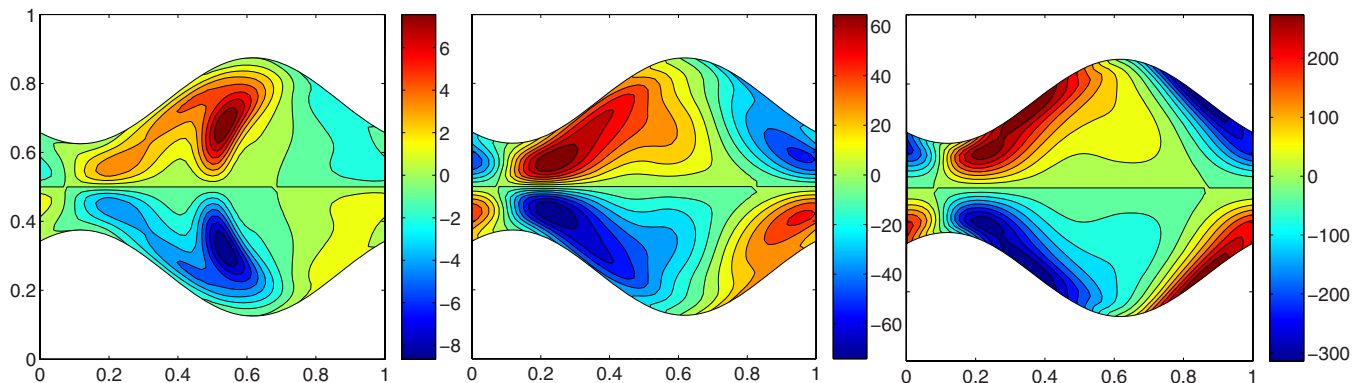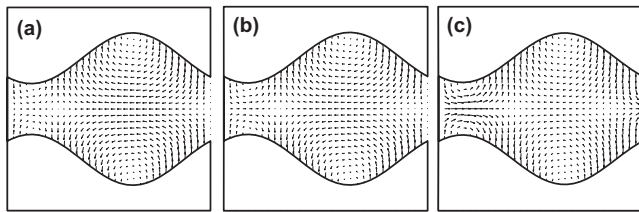
FIG. 9. The fluid velocity field in the laboratory frame at times $t_0=0.63$, $t_1=t_0+2$, and $t_2=t_0+9$, as the peristaltic wave moves from right to left.

sponds to an extensional flow across the channel. The off-diagonal stress component S_{12} shares the odd symmetry of the vorticity across the channel centerline and here increases from being initially zero, and is concentrated along the walls of the channel.

We note that while the stresses at the last time are nearly steady in the wave frame, we do observe a persistent, oscillatory low-amplitude nonsteadiness, especially in the wide part of the channel. There is no reason *a priori* that the polymer stresses should become completely steady, and it appears that they are not. Indeed, the periodicity of these oscillations is not that of the peristaltic wave and presumably reflects some other intrinsic time scale of the system.

Figure 9 shows the fluid velocity field within the channel at the same times as above. As with the vorticity, the velocity field shown at the earliest time, $t_0=0.64$ [panel (a)], is essentially that of the purely Newtonian problem. Though the changes between panel (a) (time t_0) and panel (b) (time t_0+2) are difficult to discern, the differences are important. In particular, with time the stagnation point upstream of the pump neck has shifted further upstream, reflecting a strengthening reflux in the neck. At the latest time, time t_0+9 in panel (c), this reflux backflow is fully developed and has decreased the initial mass flux by nearly two-thirds (Fig. 3). Figure 10 shows the elastic forces, $\beta \nabla \cdot \mathbf{S}_p$ in Eq. (3), created in this flow. There are several aspects worth noting. First, as would be expected from the stresses themselves, these elastic forces become large with increasing pump reflux. At the earliest time, $t=t_0$, they are not yet sufficiently large to affect the mainly Stokesian velocity field. Second, downstream (leftwards) of the pump neck these elastic forces are well aligned with the velocity field that develops and drives the reflux. Third, within the neck itself there is the appearance of large elastic forces oriented toward the moving walls. It is these large forces that we believe make it difficult to reliably simulate pumps at greater amplitude ra-
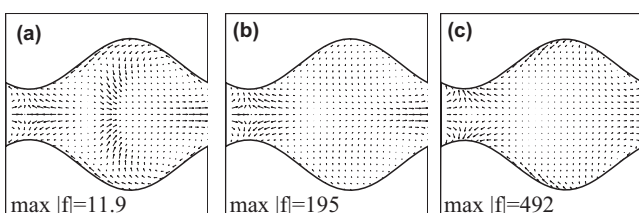

FIG. 10. The elastic force field at times $t_0=0.63$, $t_1=t_0+2$, and $t_2=t_0+9$, as the peristaltic wave moves from right to left.
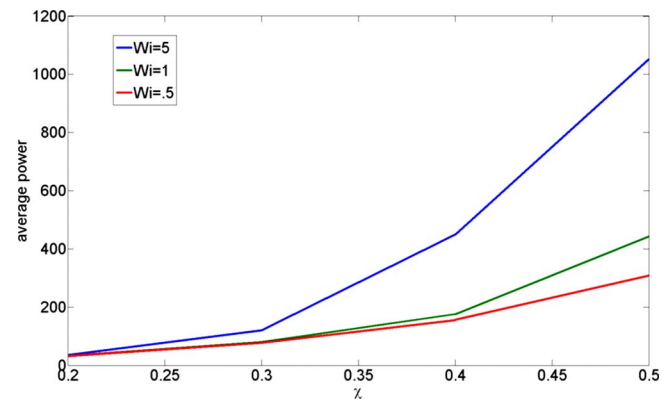

FIG. 11. (Color online) The time-averaged input power for $Wi=5$ as a function of amplitude ratio χ.

tios. Lastly, sizable elastic forces also develop asymmetrically along the walls in the wide part of the channel.

Finally, the large non-Newtonian stresses and consequent inhibiting reflux have a large effect on the input power required to drive the pump. Figure 11 shows the input power

$$\mathcal{P}(t) = \int_{\Gamma} \mathbf{v} \cdot (\mathbf{S}_s + \mathbf{S}_p) \cdot \mathbf{n} ds, \qquad (13)$$

averaged at late times after the stress growth has saturated. For all Weissenberg numbers, the power input rises with increasing amplitude ratio χ, but the rate of increase increases markedly at the larger Weissenberg number.

B. Irreversibility in Stokes-OB and its consequences

In a well-known and extraordinary scientific film, Taylor and Friedman demonstrated the consequences of reversibility of Stokes flow for a Newtonian fluid by marking a free fluid surface with "$R \ll 1$" in ink, and then slowly mixing the fluid.[27] Taylor and Friedman's statement is rendered illegible as the dye is stretched out along the surface but is returned to its original clear statement by "unmixing" the fluid through the exact reversal of the mixing procedure. In Fig. 12 we provide what we hope is as convincing an example of the *irreversibility* of the Stokes-OB equations. Following Taylor and Friedman, we mix a Stokes-OB fluid with two pegs and the track lines of material points whose positions spell out "Re ≪ 1." Unlike the Newtonian case, when the pegs reverse their orbit and return to their original positions, the statement written on the fluid remains illegible.

One interesting question is whether as the viscoelastic stresses relax in time, the words return to their original position. While we have not done that simulation, the answer is almost assuredly not due to the loss of memory in the system. However, we do note that in the $Wi \rightarrow \infty$ case, the polymer stress can be expressed exactly as

$$\mathbf{S} = \mathbf{F}\mathbf{F}^T,$$

where $\mathbf{F}$ is the deformation tensor of the flow (i.e., the Jacobian of the Lagrangian flow map). Hence, there is no loss of memory, and the polymer stress is a displacement field stress relative to the initial state. In this case, we conjecture that the
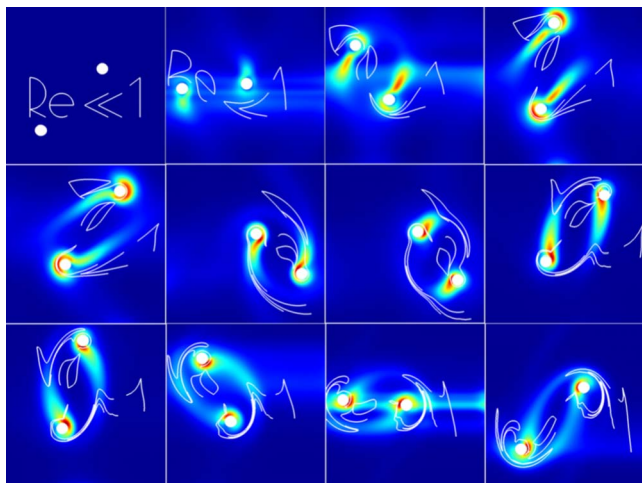
FIG. 12. (Color online) Cylindrical pegs used to mix and then unmix a Stokes-OB fluid demonstrating the loss of reversibility. The motion of the pegs is generated using tether forces. Color contours depict the normal stress in the fluid.

writing would return to its original legibility in infinite time, with the system driven there by the remaining elastic response of the fluid.

In the context of pumping, we provide yet another example of Stokes-OB irreversibility by simulating a reversing peristaltic wave. The top row of Fig. 13 shows the consequences for fluid particle transport for a Newtonian fluid that is pumped leftward for one cycle, and then backward for one cycle. The fluid particles all return to their original positions. The lower two rows show the result for Stokes-OB after five such back-and-forth cycles. The particles do not return to their original positions, and indeed the cycling appears to induce a mixing dynamics with tongues of fluid moving backward into the channel.
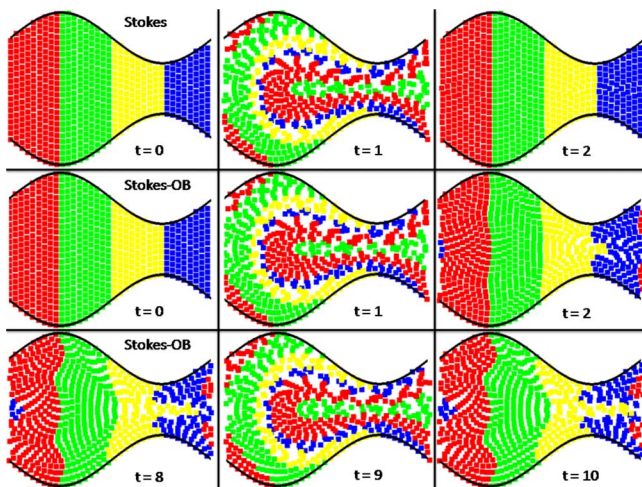

FIG. 13. (Color online) In another example of Stokes-OB irreversibility, we simulate a reversing peristaltic wave. The lower two rows show the result for Stokes-OB after five back-and-forth peristaltic cycles. The particles do not return to their original positions, and the cycling appears to induce mixing dynamics. The reversibility of a Stokesian fluid is shown for contrast in the top row. The Stokes-OB simulation was performed with $Wi=5$.

An important and interesting question is whether all non-Newtonian fluid models are necessarily irreversible. With the question carefully posed, the answer is no. One example is provided by a generalized Newtonian fluid model, a simple version of which in the Stokesian limit gives a nonlinear boundary value problem of the form [cf. Eqs. (3) and (4)]

$$-\nabla p + \nabla \cdot [\mu(\mathrm{tr}\, \mathbf{E}^2)\mathbf{E}] = -\mathbf{0} \quad \text{and} \quad \nabla \cdot \mathbf{u} = 0 \quad \text{in } \Omega,$$

$$(14)$$

with $\mathbf{u}|_{\Gamma_{1,2}} = \mathbf{v}$, where $\mathbf{E}$ is the symmetric rate-of-strain tensor. Such a model arises, for example, in the modeling of shear-thinning fluids in thin-gap flows.[28] Suppose that we solve an initial value problem on $0 \leq t \leq 2T$ and impose a reversing boundary motion by requiring that $\mathbf{v}$ reverses sign at time T, i.e., $\mathbf{v}(T+\delta) = -\mathbf{v}(T-\delta)$. It is easy to see then that the solution to Eq. (14) satisfies $(\mathbf{u}, p)_{t=T+\delta} = (-\mathbf{u}, -p)_{t=T+\delta}$, which implies reversibility of the flow itself. However, as pointed out by Goldstein, flow reversibility is not preserved by this system under all boundary deformations for which the Newtonian system preserves reversibility. For Newtonian Stokes, it is only necessary that the boundary goes forward and back through the same set of shapes, not that the boundary velocity itself reverses; reversibility is lost for a generalized Newtonian fluid if, for example, the boundary moves more quickly or slowly under reversion. This is so because the viscosity now depends nonlinearly on the fluid velocity gradients.

V. CONCLUSIONS

Numerical investigation of the peristaltic transport of a highly viscous Stokes-OB fluid over a range of Weissenberg numbers and peristalsis amplitudes demonstrates marked differences from the much studied Newtonian Stokes case. Most significantly, the fluidic transport of the pump shows a substantial decrease with the amplitude to channel separation ratio χ for large Weissenberg numbers. This decrease is in contrast to the monotonic increase with χ seen in a Newtonian fluid. Our simulations show that complex stress and vorticity patterns develop during peristalsis. The loss of reversibility inherent in the Stokes-OB model is also presented in the context of peristalsis and mixing. Even with this simple O-B model of a non-Newtonian fluid, we observe fundamentally different and complex behaviors in these classically formulated problems of fluid mechanics. A novel numerical method for viscoelastic fluid/structure interaction based on the immersed boundary method was developed to perform our investigation.

There are several interesting questions to consider in future work. One would be to consider viscoelastic flows models, such as finite extensible nonlinear elastic (FENE) or its approximation FENE-P, that limit the growth of polymer stretching.[18] Plainly, large stretching is implicated in the development of reflux and elastic forces observed here. A second very interesting direction would be to study the effect of wall geometry and pumping direction on peristaltic pumping. Here we studied only symmetric wall profiles. While wall shape affects pumping in the Newtonian case, changing the direction of the wave motion only reverses the sign of the

velocity field and hence does not affect flux. This is another aspect of Stokes reversibility. For a viscoelastic fluid, the direction of pumping does matter, as shown by Groisman and Quake[29] for pressure driven pumping in a geometrically anisotropic channel.

ACKNOWLEDGMENTS

[1] A. Fogelson, "Continuum models of platelet aggregation: Formulation and mechanical properties," SIAM J. Appl. Math. **52**, 1089 (1992).

[2] B. Schmidt-Nielsen and B. Graves, "Changes in fluid compartments in hamster renal papilla due to peristalsis in the pelvic wall," Kidney Int. **22**, 613 (1982).

[3] G. Kunz, D. Beil, H. Deiniger, A. Einspanier, G. Mall, and G. Leyendecker, "The uterine peristaltic pump. Normal and impeded sperm transport within the female genital tract," Adv. Exp. Med. Biol. **424**, 267 (1997).

[4] J. R. Blake, P. G. Vann, and H. Winet, "A model of ovum transport," J. Theor. Biol. **102**, 145 (1983).

[5] R. Jansen and K. Bajpai, "Oviduct acid mucus in the estrous rabbit: Ultrastructure and histochemistry," Biol. Reprod. **26**, 155 (1982).

[6] O. Eytan, F. Azem, I. Gull, I. Wolman, D. Elad, and A. L. Jaffa, "The mechanism of hydrosalpinx in embryo implantation," Hum. Reprod. **16**, 2662 (2001).

[7] J. C. Burns and T. Parkes, "Peristaltic motion," J. Fluid Mech. **29**, 731 (1967).

[8] M. Jaffrin and A. Shapiro, "Peristaltic pumping," Annu. Rev. Fluid Mech. **3**, 13 (1971).

[9] C. Pozrikidis, "A study of peristaltic flow," J. Fluid Mech. **180**, 515 (1987).

[10] S. Takabatake, K. Ayukawa, and A. Mori, "Peristaltic pumping in circular cylindrical tubes: A numerical study of fluid transport and its efficiency," J. Fluid Mech. **193**, 267 (1988).

[11] L. Fauci, "Interaction of oscillating filaments: A computational study," J. Comput. Phys. **86**, 294 (1990).

[12] M. J. Li and J. G. Brasseur, "Nonsteady peristaltic transport in finite-length tubes," J. Fluid Mech. **248**, 129 (1993).

[13] O. Eytan and D. Elad, "Analysis of intra-uterine fluid motion induced by uterine contractions," Bull. Math. Biol. **61**, 221 (1999).

[14] O. Eytan, A. L. Jaffa, and D. Elad, "Peristaltic flow in a tapered channel: Application to embryo transport within the uterine cavity," Med. Eng. Phys. **23**, 473 (2001).

[15] O. Eytan, D. Elad, U. Zaretsky, and A. L. Jaffa, "A glance into the uterus during in vitro simulation of embryo transfer," Hum. Reprod. **19**, 562 (2004).

[16] O. Eytan, A. J. Jaffa, J. Har-Toov, E. Dalach, and D. Elad, "Dynamics of the intrauterine fluid-wall interface," Ann. Biomed. Eng. **27**, 372 (1999).

[17] S. Yaniv, D. Elad, A. J. Jaffa, and O. Eytan, "Biofluid aspects of embryo transfer," Ann. Biomed. Eng. **31**, 1255 (2003).

[18] R. G. Larson, *The Structure and Rheology of Complex Fluids* (Oxford University Press, Oxford, 1998).

[19] P. Arratia, C. Thomas, J. Diorio, and J. Gollub, "Elastic instabilities of polymer solutions in cross-channel flow," Phys. Rev. Lett. **96**, 144502 (2005).

[20] L. Fauci, "Peristaltic pumping of solid particles," Comput. Fluids **21**, 583 (1992).

[21] C. Peskin, "The immersed boundary method," Acta Numerica **11**, 479 (2002).

[22] F. Harlow and E. Welch, "Numerical calculation of time-dependent viscous incompressible flow of fluids with free surface," Phys. Fluids **8**, 21 (1965).

[23] M. Jaffrin and A. Shapiro, "Peristaltic pumping," Annu. Rev. Fluid Mech. **3**, 13 (1971).

[24] E. Lauga, "Propulsion in a viscoelastic fluid," Phys. Fluids **19**, 083104 (2007).

[25] M. Jaffrin, A. Shapiro, and S. Weinberg, "Peristaltic pumping with long wavelengths at low Reynolds number," J. Fluid Mech. **37**, 799 (1969).

[26] B. Thomases and M. Shelley, "Emergence of singular structures in Oldroyd-B fluids," Phys. Fluids **19**, 103103 (2007).

[27] G. I. Taylor and J. Friedman, *Low Reynolds Number Flows (National Committee on Fluid Mechanics Films)* (Encyclopedia Britannica Educational, London, 1966).

[28] L. Kondic, M. Shelley, and P. Palffy-Muhoray, "Non-Newtonian Hele-Shaw flow and the Saffman–Taylor instability," Phys. Rev. Lett. **80**, 1433 (1998).

[29] A. Groisman and S. Quake, "A microfluidic rectifier: Anisotropic flow resistance at low Reynolds numbers," Phys. Rev. Lett. **92**, 094501 (2004).